RSC Sustainability

ROYAL SOCIETY OF CHEMISTRY

PAPER

View Article Online
View Journal

Cite this: DOI: 10.1039/d5su00499c

Dual-functional additives for stable perovskite thin films

Siwon Yun, †[a] Mi-Seon Bae, †[b] Muhammad Adnan, [a] Zobia Irshad, [a] Wonjong Lee, [a] Hyeji Han, [a] Tae-Youl Yang, *[b] Hyo Sik Chang, *[a] Jinseck Kim *[c] and Jongchul Lim *[a]

Organic–inorganic lead halide perovskites have emerged as frontrunners in next-generation optoelectronic technologies due to their exceptional optoelectronic properties. Despite remarkable advancements, their commercialization is hindered by their poor intrinsic stability and suboptimal charge-carrier dynamics. In this work, we introduced thionate-based additives, 1-butyl-3-methylimidazolium thiocyanate (BMIM-SCN) and 1-butyl-3-methylimidazolium lead thiocyanate (BMIM-$Pb(SCN)_3$), as effective chemical modulators to simultaneously enhance the crystallinity, surface quality, and environmental resilience of hybrid perovskite films. The incorporation of these additives facilitates the formation of dense, uniform crystal grains with improved surface coverage and significantly reduced surficial and interfacial trap states. The modified films exhibit superior charge transport behavior and demonstrate remarkable resilience under humid, thermal, and light stress, outperforming their pristine counterparts. Specifically, BMIM-$Pb(SCN)_3$ is proven to be particularly effective, synergistically enhancing both the charge-carrier mobility and long-term film stability. This dual-functional additive strategy not only passivates defects but also regulates the structural evolution of the perovskite layer, leading to an improved optoelectronic performance. These findings present a viable route for stabilizing hybrid perovskites and advancing their practical deployment in photovoltaic and optoelectronic applications.

Received 27th June 2025
Accepted 31st October 2025

DOI: 10.1039/d5su00499c

rsc.li/rscsus

Sustainability spotlight

Perovskite solar cells (PSCs) have attracted significant attention as next-generation photovoltaics due to their high efficiency and cost-effective fabrication. Their exceptional performance is primarily influenced by manipulating interfacial phenomena, which is crucial for achieving a high power conversion efficiency and stability. This study presents a comprehensive investigation into the structural, optical, and electrical stability properties of perovskite thin films employing thionate-based dual-functional additives. We elucidate their degradation properties under humid and thermal conditions using controlled and environmental conditions to gain a deeper understanding of the stability of perovskite thin films with additives, offering valuable implications for advancing optoelectronic applications. This aligns with the UN's Sustainable Development Goals, particularly Goal 7 (Affordable and Clean Energy), promoting renewable energy adoption.

1 Introduction

Since the discovery of organic-metal-halide perovskites, they have attracted widespread interest owing to their remarkable optoelectronic characteristics.[1–6] The advantages of perovskite materials include solution processability, band gap tunability, and low exciton binding energies. Moreover, perovskite materials are superior because of their long charge carrier diffusion lengths and high charge carrier mobility compared to their organic semiconductor counterparts.[7,8] Due to these advantages, perovskite solar cells (PSCs) have presented a certified power conversion efficiency of more than 26% in a single junction and 34% in tandem devices.[9–11]

Despite the significant strides in their performance, the stability of perovskites remains a concern, hindering their commercialization. In particular, surface defects in perovskites serve as active sites for degradation, where exposure to the external environment accelerates the formation of reactive species, induces trap states, and promotes structural decomposition of the perovskite lattice. Especially, humidity, heat, and light stress are responsible for the structural deformation of perovskites, resulting in the deterioration of the perovskite film phase from the photoactive to non-active phase because of crystal lattice distortion.[12–16]

[a]Graduate School of Energy Science and Technology (GEST), Chungnam National University, Daejeon, 34134, Republic of Korea. E-mail: jclim@cnu.ac.kr
[b]Department of Materials Science and Engineering, Chungnam National University, Daejeon 34134, Republic of Korea
[c]Department of Polymer-Nano Science and Technology, Department of Nano Convergence Engineering, Jeonbuk National University, Jeonju, 54896, Republic of Korea
† These authors contributed equal.

Various strategies and material modulation have been applied thus far to improve the performance and stability of PSCs. The representative strategy is the introduction of additives, dopants, or capping layers consisting of organic small molecules or polymeric materials.[17–19] Among them, the incorporation of additives is particularly attractive, as it represents one of the simplest and most mass production-compatible methods to enhance both the performance and stability of PSCs. In addition, additives contribute to the immobilization of toxic Pb^{2+} ions, which is one of the crucial issues in the sustainability of PSCs.[20,21] In this regard, previous reports have adopted additives to passivate the surface defects in perovskites, thereby improving their photovoltaic performance and stability. For instance, Zhu *et al.* employed zinc thiocyanate ($Zn(SCN)_2$) or lead(II) thiocyanate ($Pb(SCN)_2$) additives. They reported that SCN^- ions effectively enhance the optical properties and stability compared to the non-SCN-treated perovskite.[22,23] Peterozza *et al.* and Liu *et al.* also employed $Pb(SCN)_2$ additives.[24,25] They explained that the thiocyanate ion (SCN^-) passivates the surface and grain boundary defects.

Besides these studies using inorganic salt-type additives, recent efforts have focused on functional organic cations to enhance the structural stability of perovskites further. In particular, 1-butyl-3-methylimidazolium ion ($BMIM^+$) has attracted attention for its ability to stabilize the perovskite lattice and passivate defect sites by suppressing ion migration. For example, Snaith *et al.* introduced $BMIM^+$ ions into perovskite and showed that the $BMIM^+$ ions preferentially localize at the grain boundaries. $BMIM^+$ ions act as a barrier to degradation due to oxygen or moisture adsorption, thereby passivating grain boundaries, and effectively alleviating ion migration.[6] As a result, $BMIM^+$ ions help retard the degradation of perovskite even at high temperature.[26,27] Based on these previous studies, we hypothesized that the integration of $BMIM^+$ and SCN^- could exhibit a synergistic effect, not only in passivating defects but also in enhancing the structural stability of perovskite films.

Herein, we employed SCN^--based additives, 1-butyl-3-methylimidazolium thiocyanate (BMIM-SCN) and 1-butyl-3-methylimidazolium lead thiocyanate (BMIM-$Pb(SCN)_3$), to enhance the performance and stability of perovskite films by passivating their surface defect sites. In the latter, $Pb(SCN)_2$ is combined with BMIM-SCN, which helps improve the perovskite film quality and lattice stability by combining lead ions with uncoordinated anions in the perovskite crystal.[3] The insertion of additional SCN^- ions may assist in minimizing the defect density by filling the halide vacancies within the perovskite crystal lattice, helping to suppress charge-carrier recombination and elongating the photoluminescence lifetime. Furthermore, we performed a series of structural, optical, and electrical analyses to elucidate the correlation among incorporated SCN^--based additives, film homogeneity, and charge carrier dynamics. The results revealed that BMIM-SCN and BMIM-$Pb(SCN)_3$ enhanced the crystallinity of the perovskite films, suppressed trap formation, and significantly improved the charge carrier mobility, leading to remarkable resistance against air exposure and heat-induced degradation. It is particularly noteworthy that BMIM-$Pb(SCN)_3$ demonstrated a superior performance by passivating the surface and interfacial defects in the perovskite. Therefore, its charge-transporting behaviour is enhanced, which leads to an improved device performance and film stability.

2 Results and discussion

2.1 As-deposited perovskite film properties and PSC performance

The perovskite thin films were fabricated *via* a one-step solution deposition method. To ensure a consistent and reliable evaluation of the additive effects, we employed a compositionally optimized lead halide perovskite, $Cs_{0.17}FA_{0.83}Pb(I_{0.77}Br_{0.23})_3$, known for its enhanced structural and environmental stability.[6,28] This composition was specifically chosen to minimize the influence of rapid material degradation, thereby isolating the role of the thionate-based additives in modulating the crystallization behavior and performance characteristics of the film. A schematic illustration of the process for the deposition of the perovskite film is shown in Fig. 1. We demonstrate more details about the film fabrication procedure in the SI.

The modification of the crystallinity of the perovskite owing to the additives was measured using scanning electron microscopy (SEM) and X-ray diffraction (XRD). Fig. S1(a–c) illustrate the morphology of the perovskite thin films without and with additives on glass substrates. Moreover, Fig. S1(d) displays a histogram of the grain size of the corresponding films. The average grain size of the control sample is 0.284 ± 0.08 μm, that of the film with BMIM-SCN additive is 0.465 ± 0.14 μm, and the film with BMIM-$Pb(SCN)_3$ additive is 0.654 ± 0.16 μm. These results clarify that employing additives effectively increases the grain size relative to the perovskite without additives. This might be attributed to the interaction between the additives and perovskite.[3,27,29]

Fig. S2(a and b) present the XRD results, indicating that the incorporation of BMIM-SCN and BMIM-$Pb(SCN)_3$ additives enhances the crystallinity of the perovskite thin films. The control film shows a distinct PbI_2 peak at the 2θ value of around 12.5°, suggesting the presence of residual PbI_2. However, employing BMIM-SCN and BMIM-$Pb(SCN)_3$, the intensity of the PbI_2 peak is reduced, indicating the suppressed formation of PbI_2, and thus improved phase purity of the perovskite films. Furthermore, the intensity of the main perovskite (100) peak increases with the incorporation of the additives.[30]

Moreover, X-ray photoelectron spectroscopy (XPS) analysis was performed to evaluate the change in chemical bonding within the perovskite by interaction with the additives, as displayed in Fig. S2(c and d). On the as-prepared surface of the perovskite, a shift in the Pb 4f signals was detected with a slight increase in binding energy upon the incorporation of BMIM-SCN and BMIM-$Pb(SCN)_3$. In detail, the Pb $4f_{7/2}$ and Pb $4f_{5/2}$ peaks of the control perovskite films were positioned at 137.90 and 142.65 eV, respectively. The corresponding peaks were located at 137.95 and 142.70 eV for the BMIM-SCN-based film and 138.00 and 142.75 eV for the BMIM-$Pb(SCN)_3$ film, respectively. These peak shifts imply the strong chemical interaction between Pb^{2+} ions and the additives, leading to the effective

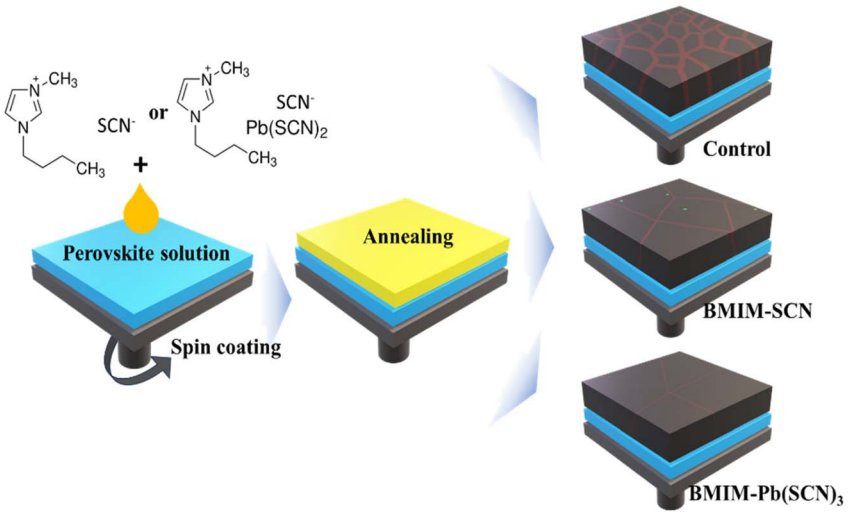

Fig. 1 Schematic of the procedure for the fabrication of the perovskite thin films without and with additives.

immobilization of Pb^{2+} ions at the perovskite surface. This effect contributed to the passivation of the dangling bonds of Pb^{2+} ions by the incorporation of additives.[3,29]

With the incorporation of the additives, the binding energy of I slightly decreased, as shown in Fig. S2(d). In the case of the control film, the I $3d_{5/2}$ and I $3d_{3/2}$ peaks were located at 617.90 and 629.40 eV, respectively. By added BMIM-SCN to the perovskite thin film, these peaks slightly shifted to a lower binding energy at 617.80 and 629.35 eV, respectively, which can be attributed to the generation of uncoordinated I^- ions on the surface during the interaction with BMIM-SCN. Meanwhile, upon treatment with BMIM-$Pb(SCN)_3$, the peaks slightly shifted to a higher binding energy (617.85 and 629.40 eV), indicating that the additional Pb^{2+} ions provided by BMIM-$Pb(SCN)_3$ effectively coordinate with the halides, respectively. These results suggest that additives cause the grain growth in the perovskite to be more uniform, forming highly crystalline perovskite films.[30–32]

In short, comparing the average grain size, crystallinity, and binding energy between the films with additives, BMIM-$Pb(SCN)_3$ contributed to improved crystalline grain growth compared to BMIM-SCN. When BMIM-SCN is incorporated into the perovskite, $BMIM^+$ ions might occupy the cation vacancies on the surface, interacting with lead and halide ions. In contrast, SCN^- ions penetrate the perovskite lattice and coordinate with anion vacancies, thereby passivating defects. In this case, the excessive lead ions in BMIM-$Pb(SCN)_3$ might facilitate coordination with residual unbound anions generated during the interaction between perovskite and BMIM-SCN, thereby facilitating more effective crystalline grain growth.[3]

We characterized the current density–voltage (J–V) curves of the as-prepared PSCs to demonstrate the effect of the additives on the photovoltaic performance. The procedure for the fabrication of the devices is presented in the SI. The performances of the PSCs without and with additives are tabulated in Table S1, and the related J–V traces and PSC characteristics are displayed in Fig. S3(a–e). The open-circuit voltage (V_{oc}) of the additive-treated PSCs was higher than that of the control. In the reverse sweep measurement, the V_{oc} of the control sample was measured to be 1.11 V, and the value for the BMIM-SCN-treated films was 1.15 V and 1.16 V for BMIM-$Pb(SCN)_3$. Furthermore, the short-circuit current-density (J_{sc}) was measured to be 20.01 mA cm^{-2} for the control, 20.18 mA cm^{-2} for BMIM-SCN, and 20.21 mA cm^{-2} for BMIM-$Pb(SCN)_3$, as shown in Fig. S3(c). The incorporation of additives increased the J_{sc}. This might result from the enhanced charge extraction due to the incorporation of the additive, which facilitates better crystalline grain growth. A similar trend was also observed in the fill factor (FF). Consequently, these enhancements contributed to the improved device performance, as displayed in Fig. S3(e). The best device performance of 17.65% was achieved in the BMIM-$Pb(SCN)_3$-treated device. This is due to the additive-induced improvement in the overall film quality, including enhanced crystallinity, which results in a better photovoltaic performance.[16,29,33–35]

2.2 Perovskite thin film performance under degraded ambient air conditions

To investigate the impact of additives on the stability of the perovskite film, we monitored the perovskite films without and with additives, upon storage for 120 h under ambient air conditions. The films were kept without encapsulation in a controlled environment at 22°C ± 3 °C and 20% ± 5% RH. We measured the charge carrier properties at a constant interval of 24 h. In addition, from 72 h of storage, thermal treatments were conducted at a constant interval of 24 h at 100 °C for 30 min to induce the redistribution of ions in the perovskite films.

To evaluate the change in optical properties during degradation under ambient air conditions, we measured steady-state photoluminescence (SSPL). Furthermore, we analyzed the time-resolved photoluminescence (TRPL) to investigate the charge carrier recombination dynamics. The corresponding data are presented in Fig. S4; the charge carrier lifetime fitting values are summarized in Table S2. We compared the SSPL intensities of

the as-prepared and aging films under ambient air conditions, as shown in Fig. S4(a–c). The SSPL intensities of the as-prepared perovskite films were highest in the order of BMIM-$Pb(SCN)_3$ > BMIM-SCN > control. A higher SSPL intensity reflects reduced non-radiative recombination, which is typically associated with defect states in the perovskite. Therefore, the results imply that the perovskite films treated with additives effectively passivate defects in the perovskite films; the effect is more pronounced in the BMIM-$Pb(SCN)_3$-treated films, as reflected by their superior SSPL intensity. In relation to this, the reduced grain boundaries observed in Fig. S1 contribute to the enhanced SSPL intensity of the additive-treated perovskite films.[16,29,31,34,36]

More importantly, the presence and type of additives led to distinct variations in the SSPL intensity over storage time, highlighting their influence on the stability of the perovskite films. As displayed in Fig. 2(a), the SSPL intensities of all the samples gradually decreased over time during ambient air storage. However, the degree of reduction varied depending on the sample. After 48 h, the SSPL intensity was reduced by 34.72%, 23.20%, and 11.36% for the control, BMIM-SCN, and BMIM-$Pb(SCN)_3$ samples, respectively. Furthermore, when we applied thermal treatments after 72 h of storage, the SSPL intensity of the control sample continued to decrease over time, whereas the degradation trend was mitigated in the BMIM-SCN-treated perovskite film. Notably, the SSPL intensity of the BMIM-$Pb(SCN)_3$-treated sample remained nearly unchanged. These findings indicate that defect passivation by additives reduces environmental (*e.g.*, moisture)-related degradation by coordination at the defect sites. In short, it can be inferred that the additives not only passivate defects in the as-prepared perovskite films but also enhance their stability against ambient air. Ultimately, after 120 h of storage, the SSPL intensity was reduced by approximately 68.54%, 58.48%, and 37.66% for the control, BMIM-SCN, and BMIM-$Pb(SCN)_3$ samples, respectively, as shown in Fig. 2(a).

In addition, we investigated the charge carrier lifetimes of the perovskite films using TRPL measurements to understand their carrier transport and recombination behaviors (Fig. S4(d and f)). To investigate the recombination rate, we applied the stretched mode instead of the mono decay mode to calculate the charge carrier lifetimes. The stretched mode allows for the estimation of the trap density, which influences the charge carrier lifetime. Near the film surface, exciton generation by incident light is immediately followed by charge carrier trapping, and the subsequent diffusion of charge carriers is delayed due to the rapid trapping process, as described by the following equation:[37]

$$I(t) = A \exp\left[-\left(\frac{t}{\tau}\right)^{\beta}\right] \quad (1)$$

where $I(t)$ is the photoluminescence (PL) intensity, t is time, A means amplitude for each value, τ denotes the calculated charge carrier lifetime, and β is the stretched exponential.[37] The results are summarized in Table S2 and depicted in Fig. 2(b). Among the as-prepared film samples, the film with BMIM-$Pb(SCN)_3$ additive presents the most extended charge carrier lifetime of 376.98 ns, followed by the film with BMIM-SCN with a value of 321.33 ns, and the control sample of 306.35 ns. After 48 h aging, the charge carrier lifetimes were reduced by 22.44%, 22.70%, and 39.00% for BMIM-$Pb(SCN)_3$, BMIM-SCN, and the control sample, respectively. Remarkably, when we applied additional heat treatment to the sample after 72 h of storage, the charge carrier lifetime exhibited recovery compared to the values at 48 h, which was more pronounced in the films with additives. After 120 h, the charge carrier lifetime was reduced by 38.56%, 50.46%, and 58.49% of the initial value for BMIM-$Pb(SCN)_3$, BMIM-SCN, and the control sample, respectively. This result implies that the perovskite film with additive effectively retards the degradation compared to the control film under ambient air. Moreover, the film employing BMIM-$Pb(SCN)_3$ is more effective for retarding degradation than the film employing BMIM-SCN additive. This behavior can be explained by the different interaction mechanisms between the additives and the perovskite. In the of case BMIM-SCN additive, SCN^- ions can penetrate into the lattice and substitute for halide sites, contributing to defect passivation. However, this process leaves residual uncoordinated halide ions in the films, which can act as trap sites. In contrast, the BMIM-$Pb(SCN)_3$ additive has excess Pb^{2+} ions, which can effectively coordinate with these unbound halide ions, thereby further stabilizing the

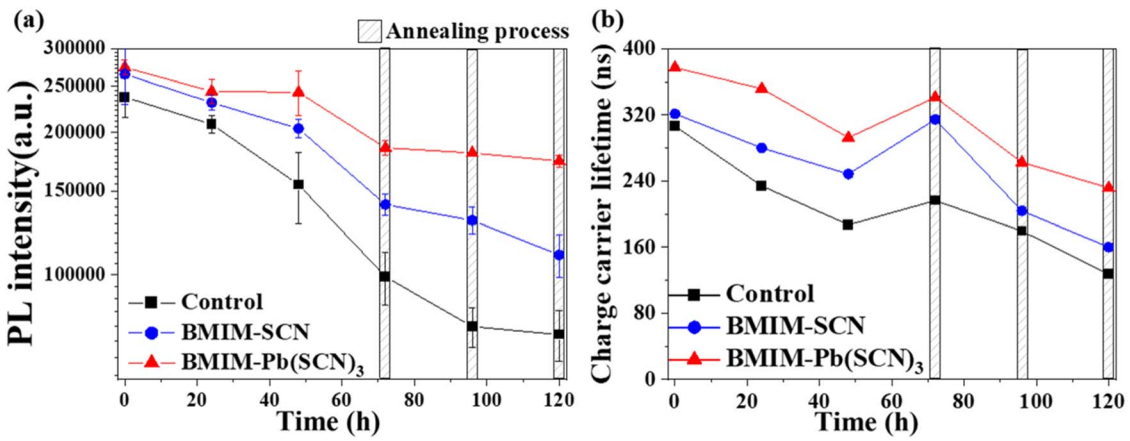

Fig. 2 Single charge carrier performance without and with additives over storage time: (a) PL intensity and (b) charge carrier lifetime.

perovskite structure.[3] As a result, the films treated with BMIM-$Pb(SCN)_3$ present excellent resistance to ambient air-induced degradation.

Furthermore, we employed the pulsed voltage space charge limited current (PV-SCLC) method to investigate the defect passivation effect of the additives in perovskites. PV-SCLC introduces pulsed voltage, unlike conventional SCLC, which applies bias continuously. Therefore, this method is advantageous in separating ionic and electronic contributions in mixed-conducting perovskites, which allows more accurate evaluation of their intrinsic electronic properties.[38,39] We observed the vertical charge carrier transport properties and defect densities of the films.[38,39] As shown in Fig. S5, all the films showed a transparent Ohmic region ($J \propto V^1$) at low voltage, where the conductivity (σ) could be determined by following the equation.[40]

$$\sigma = \frac{L}{A}\frac{1}{R} \tag{2}$$

where L is the film thickness, A is the area, and R is the resistance. Furthermore, as the applied voltage increases, the current shifts into the space charge limited current (SCLC) regime, where $J \propto V^2$. Here, we could calculate the electron mobility using the Mott–Gurney square law, as follows:[41,42]

$$J = \frac{8\varepsilon_0\varepsilon_r\mu V^2}{9L^3} \tag{3}$$

where J presents the current density, ε_0 is the permittivity of free space (8.85×10^{14} C V^{-1} cm^{-1}), and ε_r is the relative permittivity of the material.[43] In addition, μ is the mobility of the charge carriers and V is the applied voltage. Subsequently, when the voltage applied exceeds the SCLC region, the system reaches the trap-filling limited (TFL) region ($J \propto V^3$). The cross-point voltage of the SCLC and TFL is defined as V_{TFL}, and we could evaluate the total trap density in the perovskite film through the following equation:[42]

$$N_t = \frac{2V_{TFL}\varepsilon\varepsilon_0}{eL^2} \tag{4}$$

where N_t is the trap density and e is the electric charge of an electron. The result demonstrated that the electric properties under ambient air degradation varied depending on the additives, as illustrated in Fig. S5(a–c). The electric properties are summarized in Table S3 and Fig. 3(a–c).

The as-prepared control sample exhibited the lowest electrical performance, with a conductivity of $4.88 \pm 0.25 \times 10^{-9}$ S cm^{-1} and an electron mobility of $1.92 \pm 0.30 \times 10^{-4}$ cm^2 V^{-1} s^{-1}. Its corresponding trap density was calculated to be $7.42 \pm 0.51 \times 10^{15}$ cm^{-3}. In contrast, the perovskite films with BMIM-SCN presented higher conductivity of $2.90 \pm 0.26 \times 10^{-8}$ S cm^{-1} and electron mobility of $9.09 \pm 0.33 \times 10^{-4}$ cm^2 V^{-1} s^{-1} with a lower trap density of $6.57 \pm 0.29 \times 10^{15}$ cm^{-3}. The BMIM-$Pb(SCN)_3$-treated film exhibited the highest performance, with a conductivity of $4.68 \pm 0.69 \times 10^{-8}$ S cm^{-1}, electron mobility of $1.25 \pm 0.50 \times 10^{-3}$ cm^2 V^{-1} s^{-1}, and trap density of $5.47 \pm 0.20 \times 10^{15}$ cm^{-3}. Therefore, we could conclude that the additives passivate the defects in perovskite. Furthermore, the passivation by BMIM-$Pb(SCN)_3$ is better than that by BMIM-SCN, and they both have enhanced electrical properties.

After 48 h storage under ambient air conditions, the films were aged, and the conductivities of the films decreased by around 97.25%, 83.65%, and 78.91% for the control, BMIM-SCN, and BMIM-$Pb(SCN)_3$ treated samples, respectively (Fig. 3(a)). By 120 h, the degradation progressed further, with conductivity reduction of 94.49%, 90.55%, and 86.37% for each corresponding sample, respectively. Notably, when thermal treatment was applied after storage for 72 h, the conductivity of the films with additives increased significantly compared to the 48 h condition. This tendency corresponds well with the earlier results for the charge carrier lifetime and implies that the films containing additives experienced less severe degradation under exposure to ambient air.

Similarly, the electron mobility showed an analogous decreasing trend to the conductivity. After 48 h of storage, the electron mobility of the control, BMIM-SCN, and BMIM-$Pb(SCN)_3$ samples decreased by 59.37%, 58.64%, and 52.56%, respectively. Finally, after 120 h of storage, the mobility decreased by 93.75%, 92.93%, and 92.16% for the corresponding samples. After 72 h of storage, the recovery of electron mobility following thermal treatment was also more pronounced in the films containing additives. It can be seen that in the case of both characteristics, degradation of the films is retarded due to the introduction of the additives.

The calculated trap density provides a comprehensive representation of the observed electronic properties. Although the trap densities of all the samples increased after 48 h of storage, the extent of this increase varied depending on the presence and type of additive. In detail, after 48 h of storage, the trap density increased by 32.34%, 28.61%, and 24.68% for control, BMIM-SCN, and BMIM-$Pb(SCN)_3$ samples, respectively. In addition, after 120 h, the trap density increased to 232.88%, 198.33%, and 128.52%, respectively. Remarkably, the control sample showed a rapid trap increment after the first thermal treatment at 72 h. This behavior demonstrates that thermal stress could cause defect formation in the intrinsic perovskite. In contrast, the perovskite films with additives displayed a retarded increase in trap densities compared to the control film. In particular, the BMIM-$Pb(SCN)_3$-treated film showed the lowest trap density throughout the degradation process, indicating more effective defect passivation compared to the other samples.

Fig. 3(d–f) represent a schematic of the perovskite film without and with additives, respectively. According to the SEM images (Fig. S1(a–c)), PL and the SCLC analysis, the results indicate that the incorporation of additives plays a role in forming not only a larger grain size but also in passivating the defects. Therefore, the control sample exhibits a higher level of grain boundaries compared to the additive-treated films, as illustrated in Fig. 3(d). When BMIM-SCN is introduced into the perovskite, the SCN^- ions help passivate the defect sites; however, some uncoordinated I^- ions may remain on the surface.[3] In contrast, BMIM-$Pb(SCN)_3$ not only allows SCN^- ions to participate in defect passivation but also provides additional

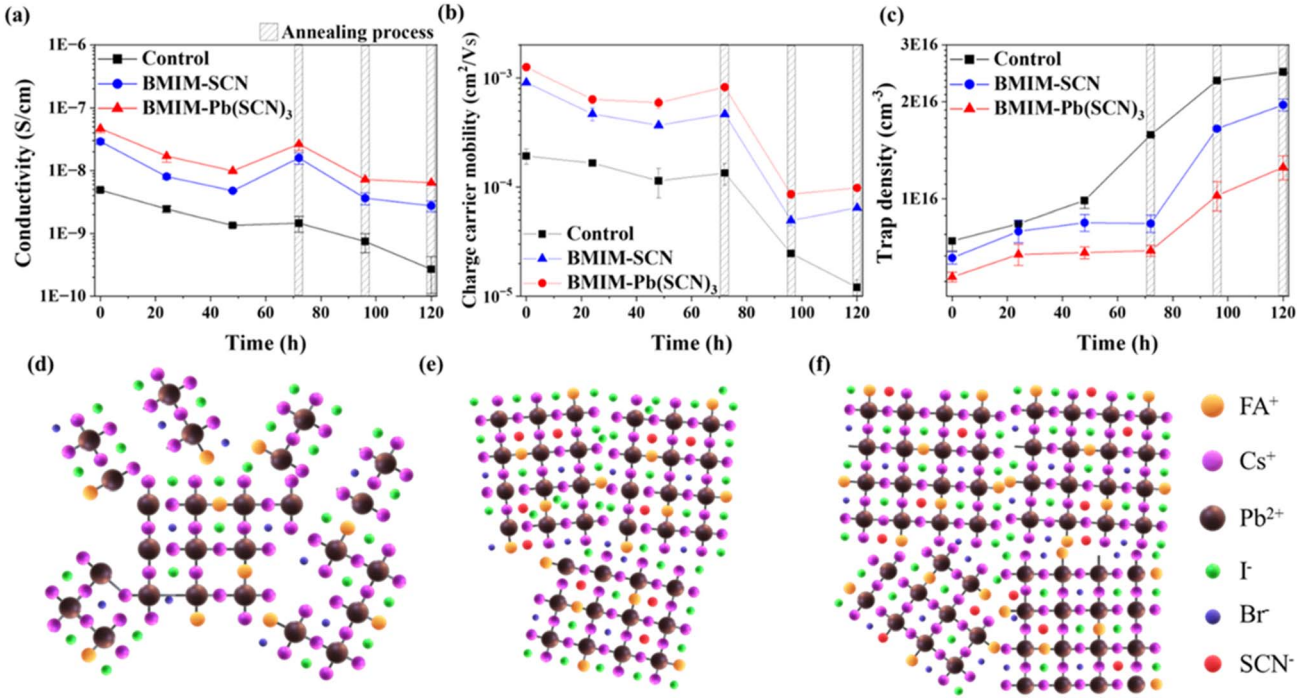

Fig. 3 The electrical properties over storage time: (a) conductivity, (b) electron mobility, and (c) the trap density. Schematic perovskite film (d) without, with (e) BMIM-SCN, and with (f) BMIM-$Pb(SCN)_3$ additives.

Pb^{2+} ions, which coordinate with unbound I^- anions, leading to more complete defect passivation within the lattice. As a result, the BMIM-$Pb(SCN)_3$-treated perovskite film exhibits improved optoelectronic properties.[44–46]

We conducted transient photoconductivity (TPC) measurements to investigate the in-plane charge carrier mobility under illumination conditions.[8] The TPC method suggests the accurate free charge carrier density under varying laser intensities, accounting for recombination and excitation carrier density. For the TPC measurements, the samples were fabricated with a configuration of glass/perovskite/Au. Photo-conductivity was calculated using the following equation:

$$\sigma_{\text{photo}} = \left(\frac{V_R}{R_R(V_{APP} - V_R)}\right)\left(\frac{l}{w \times L}\right) \quad (5)$$

where σ_{photo} is the photo-conductivity, V_R is the monitored voltage, R_R is the applied resistor, V_{APP} is the applied voltage, l is the channel-to-channel length, w is the channel width, and L is the length. In addition, we calculated the charge mobility using photo-conductivity (σ_{photo}) and the following equation:

$$\sigma_{\text{photo}} = eI_{\text{tot}}\Phi\sum\mu \quad (6)$$

where $\Phi\sum\mu$ represents the sum of the mobility of electrons and holes and I_{tot} is the total excitation charge carrier density. As shown in Fig. 4(a) and S6(a–c), we calculated the photo-conductivities and mobility without and with additives by varying the light intensity and storage time. Furthermore, we represent the measured data in Fig. S7–S9. In addition, we tabulated the calculated photo-conductivity and mobility values in Table S4. The photo-conductivity of the as-prepared films increased in the order of control < BMIM-SCN < BMIM-$Pb(SCN)_3$, with the corresponding values of $1.28 \pm 0.09 \times 10^{-2}$ S cm^{-1}, $2.30 \pm 0.25 \times 10^{-2}$ S cm^{-1}, and $2.52 \pm 0.15 \times 10^{-2}$ S cm^{-1} at the free charge carrier density of 3.47×10^{17}, respectively (Fig. 4(a)). After 120 h of storage, the perovskite films showed degradation of 85.88%, 74.65%, and 58.75% for the control, BMIM-SCN, and BMIM-$Pb(SCN)_3$, respectively. The mobility of the as-prepared films also followed the same trend as the photo-conductivity, showing higher values with the introduction of additives (control: $2.50 \pm 0.22 \times 10^{-1}$ cm^2 V^{-1} s^{-1}, BMIM-SCN: $3.97 \pm 0.15 \times 10^{-1}$ cm^2 V^{-1} s^{-1}, and BMIM-$Pb(SCN)_3$: $4.36 \pm 0.37 \times 10^{-1}$ cm^2 V^{-1} s^{-1}), respectively. The decrease in mobility over the storage was the most pronounced in the control sample (88.90%), while the sample containing BMIM-$Pb(SCN)_3$ (58.84%) exhibited the most moderate decline. The mobility in the BMIM-SCN-treated perovskite film decreased by 74.65%. The improved stability of photo-conductivity and mobility in the films containing BMIM-SCN and BMIM-$Pb(SCN)_3$ is likely due to their larger grain size and more efficient passivation of defect sites at their grain boundaries.[35,47]

Fig. 4(b) presents a schematic illustration of the charge carrier behavior upon laser illumination in the perovskite films. Both the PV-SCLC and TPC results reveal that in the control film, the presence of a high density of trap states significantly impedes the diffusion of charge carriers, leading to limited mobility and conductivity. This limitation is attributed to the presence of defects, which act as recombination centers, restricting effective charge transport. In contrast, the

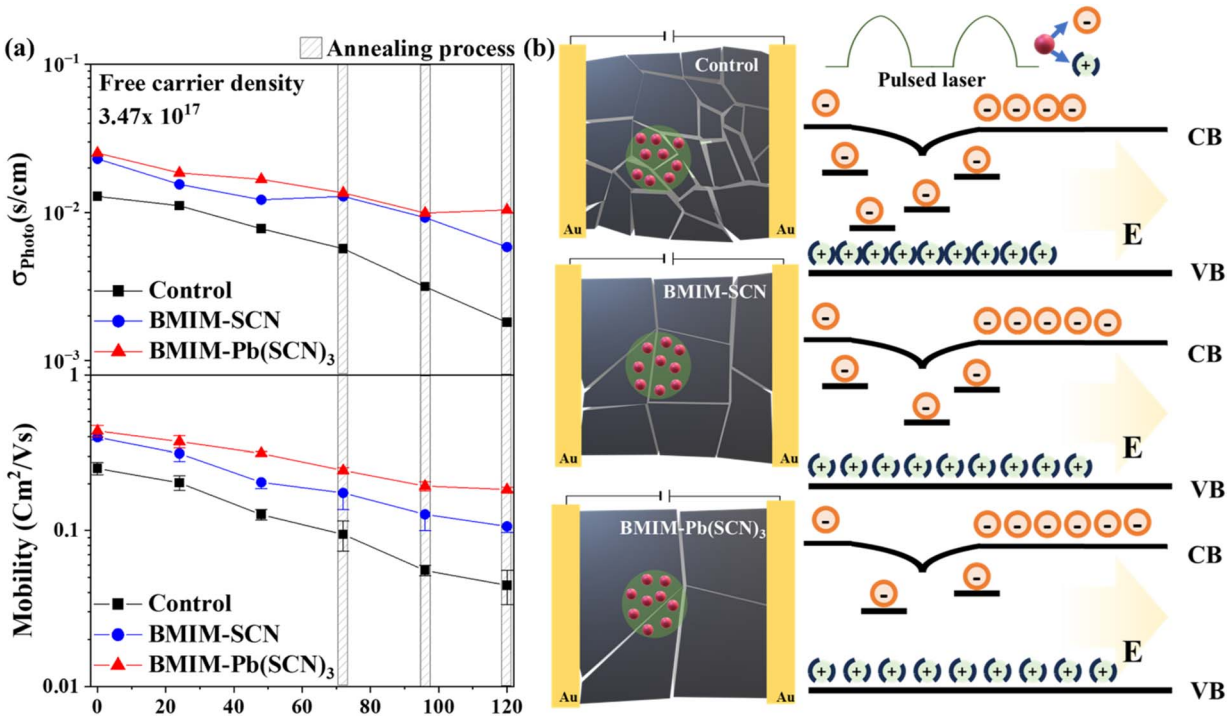

Fig. 4 The charge carrier properties of in-plane perovskite film with TPC measurement. (a) The calculated mobility and photo-conductivity using the TPC method and (b) schematic of the perovskite films with and without additives and the charge carrier mobility inside the film.

introduction of additives effectively enhances the charge carrier mobility by passivating trap states. The BMIM-SCN additive improves the charge carrier mobility, with the support of a larger grain size, which reduces the grain boundaries. BMIM-$Pb(SCN)_3$ exhibits the most pronounced enhancement in charge transport, which can be attributed to its additional functionality in the perovskite film. The excessive Pb^{2+} ions in BMIM-$Pb(SCN)_3$ facilitate coordination with residual unbound anions that are produced from the interaction between BMIM-SCN and the perovskite, leading to more effective passivation of the trap states and crystalline grain growth. As a result, non-radiative recombination was suppressed, and carrier mobility and conductivity were further improved.

2.3 Structure degradation by thermal stress

We elucidate the impact of additives on the thermal degradation of perovskite films. The film samples without or with additives were annealed at 150 °C for 16 h in an ambient air atmosphere. Fig. 5(a) shows the images of the perovskite film without and with additives, varying the heat exposure time. Hybrid perovskites are known to decompose under thermal stress conditions to form lead-halide and cation-halide.[48] Especially, upon annealing, degradation of the films occurs owing to the release of the formamidinium ion (FA^+) and iodine ion (I^-).[49] Therefore, over time, the perovskite films decomposed and turned yellow, showing the reduction of the α-phase.[50]

Notably, the films with additives showed retarded structural degradation. It is assumed that incorporating additives contributes to the accumulation of $BMIM^+$ ions at the grain boundaries of the perovskite. These ions might inhibit halide migration, particularly the release of I^- ions, thereby contributing to enhanced thermal stability.[32] As a result, when the perovskite films were exposed to high temperature at 150 °C, the samples with BMIM-SCN and BMIM-$Pb(SCN)_3$ additive displayed better film stability.

To further investigate the thermal stability of the perovskite films, we observed their optical properties using photoluminescence and ultraviolet-visible absorption spectroscopy (UV-vis) at 4 h intervals, as shown in Fig. 5(b) and (c) and S10(a–f). We traced the PL maximum peak wavelength shift, as displayed in Fig. 5(b). The control film exhibited an initial PL peak at 740 nm, which shifted to 700 nm after 16 h of heat treatment (40 nm shift). In the case of the BMIM-SCN-treated film, the peak shifted from 737 to 717 nm (20 nm shift), whereas for the BMIM-$Pb(SCN)_3$-treated film, it shifted from 738 to 720 nm (18 nm shift). This blue shift in the PL peak is attributed to the thermal degradation of the perovskite structure, especially owing to the change in the halide composition.[51] In detail, thermal stress tends to cleave the weak Pb–I bonds to form Br^--rich domains because Pb–Br bonds are shorter and stronger than Pb–I bonds.[49,52,53] As a result, a blue shift in the PL emission is observed upon prolonged heat exposure.

Along with the observed PL blue shift, the bandgap of the perovskite also increased under sustained thermal stress. Fig. 5(c) presents the Tauc plots for extrapolating the optical bandgap obtained from UV-vis absorption of perovskite films, without and with additives. The band gaps of all the samples gradually increased when the perovskite films were exposed to

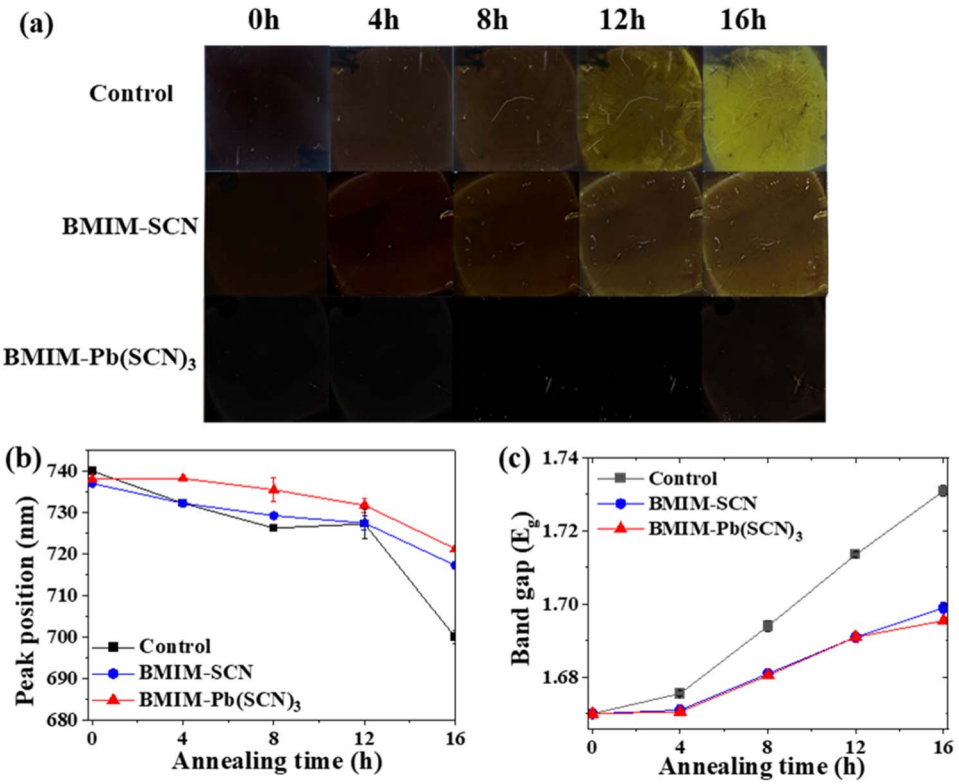

Fig. 5 (a) Morphological change in the perovskite films without and with additives during thermal treatment (annealing at 150 °C for 16 h in ambient air). (b) PL maximum peak position and (c) optical band gap, both derived from the corresponding samples shown in (a).

150 °C conditions. In the case of the as-prepared films, all the perovskites showed a band gap of 1.67 eV. When the films were aged under heat treatment, their band gaps exhibited distinct changes depending on the sample. The control sample showed a rapid increase in band gap from 1.67 to 1.73 eV; on the other hand, the BMIM-Pb(SCN)$_3$-treated sample presented the lowest increase in bandgap from 1.67 to 1.69 eV. The bandgap of the film with BMIM-SCN increased from 1.67 to 1.70 eV. In conclusion, the control sample showed rapid structural degradation due to thermal stress. Conversely, the introduction of additives hindered the structural distortion. Following the thermal stress analysis, the results suggest that the introduction of additives enhances not only the air stability but also the thermal stability by defect passivation and prevention of the breakdown of Pb–I bonds. In particular, the BMIM-Pb(SCN)$_3$ additive was more effective in preventing the degradation of perovskite from outside air and thermally stressed conditions.

2.4 Structure degradation by light stress

To elucidate the light-induced stability of the perovskite films without and with additives, we employed time-resolved photoluminescence quantum yield (PLQY). PLQY measurements were conducted at 5-min intervals for 1 h under continuous 532 nm laser exposure. The corresponding data are presented in Fig. S11. We calculated PLQY using the following equation.[54]

$$\mathrm{PLQY}(\eta) = \frac{P_\mathrm{d} - (1 - A)P_\mathrm{c}}{L_\mathrm{b}A} \quad (7)$$

$$A = 1 - \frac{L_\mathrm{d}}{L_\mathrm{c}} \quad (8)$$

where L_b is the integrated intensity of the laser signal without the sample. L_c is the integrated intensity for the laser signal with the sample located obliquely and L_d is the integrated intensity for the laser signal with the sample located as upright. P_c is the photoemission signal from the indirect sample and P_d is the photoemission signal from the direct sample.

The PL maximum peak position of all the as-prepared film samples was initially observed at 753 nm, as shown in Fig. 6(a) and S11. After 1 h of illumination, this peak exhibited a red shift for the control sample, BMIM-SCN and BMIM-Pb(SCN)$_3$ to 768, 764, and 760 nm, respectively. The control sample exhibits the largest peak shift to longer wavelengths, which is characteristic of phase segregation, where the PL emission originates from I-rich domains.[55] In contrast, the smaller peak shifts observed for the additive-treated films indicate that both BMIM-SCN and BMIM-Pb(SCN)$_3$ effectively suppress photo-induced phase segregation, thereby retarding photodegradation.[56]

Moreover, as shown in Fig. 6(b) and (c), the film with BMIM-Pb(SCN)$_3$ additive represents the highest peak intensity and PLQY compared to BMIM-SCN and the control film, respectively. Under the preparation conditions, BMIM-Pb(SCN)$_3$ shows the highest PLQY of 0.69%, followed by the BMIM-SCN film with 0.51%, and the control sample with 0.21%. This result suggests that employing additives effectively passivates defects and suppresses charge recombination.

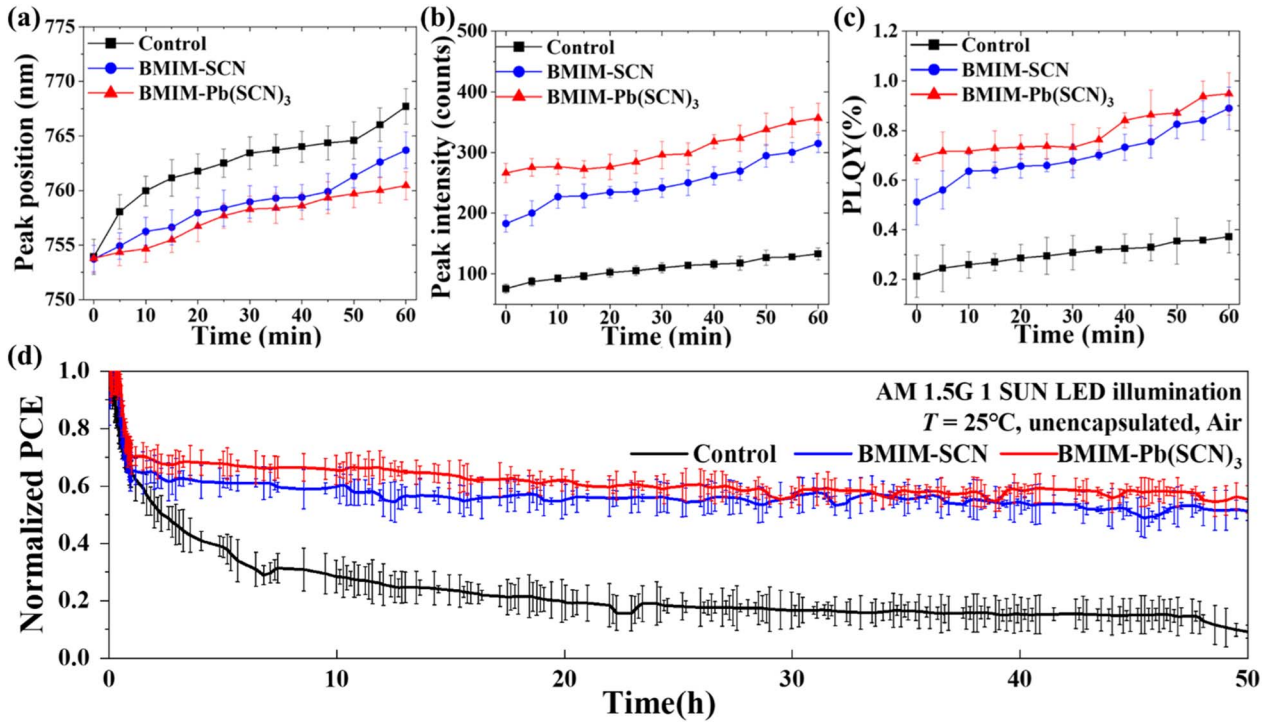

Fig. 6 Change in optical properties under light illumination over time. (a) PL maximum peak position, (b) PL maximum peak intensity, (c) calculated time-resolved PLQY, and (d) normalized PCE of PSCs without and with additives obtained from MPP measurement of unencapsulated PSCs at RT.

Upon 1 h of continuous illumination, a notable increase in PL intensity was observed across all samples. The PL intensity of the control sample increased by 76.23%, while that of the BMIM-SCN sample increased by 73.34%. Among them, BMIM-$Pb(SCN)_3$ sample showed a more moderate increase of 37.13% in PL intensity under the same illumination conditions. Similarly, the change in PLQY was investigated during 1 h of illumination for all the samples. The PLQY of the control sample increased by 75.24%, that of the BMIM-SCN treated sample by 72.94%, while the BMIM-$Pb(SCN)_3$ treated sample show an increase in PLQY of 34.79%.

Under illumination conditions, the control sample might have undergone pronounced phase segregation, as explained earlier, leading to the formation of an I^--rich phase. This compositional change resulted in the most significant increase in peak intensity compared to the additive-treated samples, as I^--rich domains are known to possess higher radiative efficiency due to photogenerated carriers relaxing into lower energy states, which promotes enhanced radiative electron–hole recombination.[57] Conversely, the BMIM-SCN- and BMIM-$Pb(SCN)_3$-treated samples successfully suppressed phase segregation compared to the control sample under illumination, as depicted in Fig. 6(a). Consequently, the moderate increase in both peak intensity and PLQY of the additive-treated samples indicate their contribution to enhancing light-phase stability and suppressing recombination.[58,59]

Furthermore, the operational durability of the devices was elucidated by maximum power point (MPP) tracking under 1 Sun (AM 1.5G) illumination (Fig. S12). In addition, the normalized MPP-tracked PCEs of the PSCs are displayed in Fig. 6(d). The control devices experienced a rapid decrease in stabilized power output, with performance retention falling below 60% within just half an hour. In contrast, the PSCs incorporating BMIM-SCN maintained its performance above 60% for up to 7 h. Furthermore, the devices with BMIM-$Pb(SCN)_3$ sustained their performance for as long as 27 h. The efficient passivation of defect sites employing BMIM-SCN and BMIM-$Pb(SCN)_3$ additives results in enhanced light and operational stability. Consequently, BMIM-SCN, and more significantly the BMIM-$Pb(SCN)_3$ additive tend to sustain the perovskite quality under ambient air, thermal, and light stress conditions.

3 Conclusion

In conclusion, we elucidated the impact of BMIM-SCN or BMIM-$Pb(SCN)_3$ additive in enhancing the performances and stability of $Cs_{0.17}FA_{0.83}Pb(I_{0.77}Br_{0.23})_3$ perovskite thin film devices. Through a variety of structural, optical, and optoelectronic analyses, we found that the incorporation of the additives significantly improved the crystallinity and uniformity of the perovskite films, thereby enhancing their photovoltaic performance and stability. When exposed to air, we specifically monitored the photoluminescence intensity, charge-carrier lifetime, mobility, and trap density to investigate the effects of additives on suppressing degradation. Notably, BMIM-$Pb(SCN)_3$ exhibited a superior performance in retarding air stress-

induced degradation. This is attributed to its dual functionality, where the SCN^- ions compensate for halide vacancies and excess Pb^{2+} ions coordinate with residual halide ions. Transient photoconductivity measurements further confirmed the effect of the incorporation of the additives, presenting the enhanced photoconductivity and charge carrier mobility of the additive-treated films. Additionally, the structural degradation of the films under thermal stress was evaluated by monitoring their PL spectra and bandgap changes. The smaller spectral shifts observed in the additive-treated perovskite films indicate the suppression of Pb–I bond cleavage in the lattice, suggesting effective retardation of thermal decomposition. Furthermore, the additives retarded phase segregation during the light illumination. This work not only highlights the potential of these additives in enhancing the performance of perovskites but also paves the way for the fabrication of highly stable perovskite thin films, showing the possibility of the commercialization of PSCs.

Author contributions

S. Y. and M. B. contributed equally to this work, conceptualized and designed the overall experiments, and wrote the original manuscript draft. W. L., M. A. provided supervision, reviewed, and edited the manuscript. H. H. and Z. I. contributed to the discussion and writing of the paper. T. Y., H. J., J. K., and J. L. contributed to supervision, resources, funding acquisition, and manuscript writing and editing. All authors have read and agreed to the published version of the manuscript.

Conflicts of interest

There are no conflicts to declare.

Data availability

All the data have been provided here and in the supplementary information (SI). Supplementary information is available. See DOI: **https://doi.org/10.1039/d5su00499c**.

Acknowledgements

This work was supported by the National Research Foundation of Korea (NRF) grant funded by the Korea government (MSIT) (No. 2023R1A2C2005172 and RS-2024-00408917). Moreover, this work was supported by the Korea Institute of Energy Technology Evaluation and Planning (KETEP) and the Ministry of Trade, Industry & Energy (MOTIE) of the Republic of Korea (No. RS-2023-00236664)

References

1 X. Cao, L. Hao, G. Su, X. Li, T. Dong, P. Chao, D. Mo, Q. Zeng, X. He and J. Wei, *RSC Sustain.*, 2023, **1**, 1290–1297.
2 H. Cho, S. H. Jeong, M. H. Park, Y. H. Kim, C. Wolf, C. L. Lee, J. H. Heo, A. Sadhanala, N. S. Myoung, S. Yoo, S. H. Im, R. H. Friend and T. W. Lee, *Science*, 2015, **350**, 1222–1225.
3 M. S. Bae, Y. H. Chang, W. Lee, C. S. Moon, S. W. Kim, H. S. Kim, J. Lim and T. Y. Yang, *Energy Fuels*, 2023, **37**, 4608–4615.
4 W. Kim, J. W. Park, Y. Aggarwal, S. Sharma, E. H. Choi and B. Park, *Nanomaterials*, 2023, **13**(3), 619.
5 M. Adnan, W. Lee, Z. Irshad, S. Kim, S. Yun, H. Han, H. S. Chang and J. Lim, *Small*, 2024, 1–13.
6 Y.-H. Lin, N. Sakai, P. Da, J. Wu, H. C. Sansom, A. J. Ramadan, S. Mahesh, J. Liu, R. D. J. Oliver, J. Lim, L. Aspitarte, K. Sharma, P. K. Madhu, A. B. Morales, Vilches, P. K. Nayak, S. Bai, F. Gao, C. R. M. Grovenor, M. B. Johnston, J. G. Labram, J. R. Durrant, J. M. Ball, B. Wenger, B. Stannowski and H. J. Snaith, *Science*, 2020, **369**, 96–102.
7 J. Wu, H. Cha, T. Du, Y. Dong, W. Xu, C. T. Lin and J. R. Durrant, *Adv. Mater.*, 2022, **34**(2), 2101833.
8 J. Lim, M. Kober-Czerny, Y. H. Lin, J. M. Ball, N. Sakai, E. A. Duijnstee, M. J. Hong, J. G. Labram, B. Wenger and H. J. Snaith, *Nat. Commun.*, 2022, **13**, 1–9.
9 Y. Wang, S. Akel, B. Klingebiel and T. Kirchartz, *Adv. Energy Mater.*, 2024, **14**(5), 2302614.
10 Z. Ying, X. Yang, X. Wang and J. Ye, *Adv. Mater.*, 2024, **36**(37), 2311501.
11 H. Chen, C. Liu, J. Xu, A. Maxwell, W. Zhou, Y. Yang, Q. Zhou, A. S. R. Bati, H. Wan, Z. Wang, L. Zeng, J. Wang, P. Serles, Y. Liu, S. Teale, Y. Liu, M. I. Saidaminov, M. Li, N. Rolston, S. Hoogland, T. Filleter, M. G. Kanatzidis, B. Chen, Z. Ning and E. H. Sargent, *Science*, 2024, **384**, 189–193.
12 J. Kim, A. J. Yun, B. Park and J. Kim, *EcoMat*, 2023, **5**, 1–11.
13 R. Sharma, Q. Zhang, L. L. Nguyen, T. Salim, Y. M. Lam, T. C. Sum and M. Duchamp, *ACS Nanosci. Au*, 2023, **3**, 230–240.
14 L. Grater, M. Wang, S. Teale, S. Mahesh, A. Maxwell, Y. Liu, S. M. Park, B. Chen, F. Laquai, M. G. Kanatzidis and E. H. Sargent, *J. Phys. Chem. Lett.*, 2023, **14**, 6157–6162.
15 D. Hirotani, K. Nishimura, K. Hamada, M. A. Kamarudin, S. Iikubo, Q. Shen, T. Toyoda and S. Hayase, *Jpn. J. Appl. Phys.*, 2021, **60**(3), 035001.
16 J. L. Miró-Zárate, M. C. Elías-Espinosa, F. Cervantes-Sodi and C. J. Diliegros-Godines, *Crystals*, 2023, **13**, 1–12.
17 A. Farag, T. Feeney, I. M. Hossain, F. Schackmar, P. Fassl, K. Küster, R. Bäuerle, M. A. Ruiz-Preciado, M. Hentschel, D. B. Ritzer, A. Diercks, Y. Li, B. A. Nejand, F. Laufer, R. Singh, U. Starke and U. W. Paetzold, *Adv. Energy Mater.*, 2023, **13**(8), 2203982.
18 D. K. Lee and N. G. Park, *Appl. Phys. Rev.*, 2023, **10**, 011308.
19 A. K. Kamali, N. M. Keppetipola, Y. Yoshihara, A. K. Jena, S. Uchida, H. Segawa, G. Sonnemann, T. Toupance and L. Cojocaru, *RSC Sustain.*, 2024, 3036–3046.
20 D. P. McMeekin, S. Mahesh, N. K. Noel, M. T. Klug, J. C. Lim, J. H. Warby, J. M. Ball, L. M. Herz, M. B. Johnston and H. J. Snaith, *Joule*, 2019, **3**, 387–401.
21 M. A. Butt, *Coatings*, 2022, **12**, 1115.
22 S. Thapa, G. C. Adhikari, H. Zhu and P. Zhu, *J. Alloys Compd.*, 2021, **860**, 158501.

23 C. Dzorkpata, S. Thapa, H. Zhu, A. Grigoriev, D. Babaian, S. Guha and P. Zhu, *J. Alloys Compd.*, 2024, **1005**, 176064.
24 S. Martani, Y. Zhou, I. Poli, E. Aktas, D. Meggiolaro, J. Jiménez-López, E. L. Wong, L. Gregori, M. Prato, D. Di Girolamo, A. Abate, F. De Angelis and A. Petrozza, *ACS Energy Lett.*, 2023, **8**, 2801–2808.
25 H. Xie, B. Zheng, C. Gao, J. Xu, J. Zhang, C. Gao and X. Liu, *RSC Adv.*, 2021, **11**, 1976–1983.
26 J.-W. Lee, S. Tan, S. Il Seok, Y. Yang and N.-G. Park, *Science*, 2022, **375**, 6583.
27 S. Bai, P. Da, C. Li, Z. Wang, Z. Yuan, F. Fu, M. Kawecki, X. Liu, N. Sakai, J. T. W. Wang, S. Huettner, S. Buecheler, M. Fahlman, F. Gao and H. J. Snaith, *Nature*, 2019, **571**, 245–250.
28 M. Lee, J. Lim, E. Choi, A. M. Soufiani, S. Lee, F. Ma, S. Lim, J. Seidel, D. H. Seo, J. Park, W. Lee, J. Lim, R. F. Webster, J. Kim, D. Wang, M. A. Green, D. Kim, J. H. Noh, X. Hao and J. S. Yun, *Adv. Mater.*, 2024, **36**(41), 2402053.
29 P. Y. Lin, C. F. Lin, Y. Y. Chiu, H. H. Chen, M. H. Li, R. Raja, C. S. Wu, C. H. Hou, S. Sung-Yun Hsiao, J. J. Shyue, D. C. Lee, S. Z. Ho, Y. C. Chen and P. Chen, *ACS Appl. Energy Mater.*, 2023, **6**, 79–88.
30 B. Ding, Y. Ding, J. Peng, J. Romano-deGea, L. E. K. Frederiksen, H. Kanda, O. A. Syzgantseva, M. A. Syzgantseva, J.-N. Audinot, J. Bour, S. Zhang, T. Wirtz, Z. Fei, P. Dörflinger, N. Shibayama, Y. Niu, S. Hu, S. Zhang, F. F. Tirani, Y. Liu, G.-J. Yang, K. Brooks, L. Hu, S. Kinge, V. Dyakonov, X. Zhang, S. Dai, P. J. Dyson and M. K. Nazeeruddin, *Nature*, 2024, **628**, 299–305.
31 D. Y. Heo, T. H. Lee, A. Iwan, L. Kavan, M. Omatova, E. Majkova, K. Kamarás, H. W. Jang and S. Y. Kim, *J. Power Sources*, 2022, **485**, 228067.
32 M. Ebic, F. Sadegh, M. Ans, D. Prochowicz, P. Yadav, S. Satapathi and S. Akin, *Small*, 2024, **20**(44), 2404190.
33 Z. Zhang, W. Chen, X. Jiang, J. Cao, H. Yang, H. Chen, F. Yang, Y. Shen, H. Yang, Q. Cheng, X. Chen, X. Tang, S. Kang, X. M. Ou, C. J. Brabec, Y. Li and Y. Li, *Nat. Energy*, 2024, **9**, 592–601.
34 Z. Zhang, Y. Zhou, Y. Cai, H. Liu, Q. Qin, X. Lu, X. Gao, L. Shui, S. Wu and J. M. Liu, *J. Power Sources*, 2018, **377**, 52–58.
35 X. Wang, H. Huang, S. Du, P. Cui, Z. Lan, Y. Yang, L. Yan, J. Ji, B. Liu, S. Qu, Q. Zhang, X. Yue, X. Zhao and M. Li, *Sol. RRL*, 2022, **6**, 1–7.
36 D. He, X. Xu, Z. Liang, Y. Niu, Y. Sun, T. Gavin, P. Falaras and L. Hu, *J. Mater. Chem. C*, 2021, **9**, 9584–9591.
37 G. Kang, J. S. Yoon, G. W. Kim, K. Choi, T. Park, R. H. Baek and J. Lim, *J. Mater. Chem. A*, 2019, **7**, 25838–25844.
38 E. A. Duijnstee, J. M. Ball, V. M. Le Corre, L. J. A. Koster, H. J. Snaith, J. Lim, E. A. Duijnstee, J. M. Ball, V. M. Le Corre, L. Jan Anton Koster, H. J. Snaith, J. Lim, E. A. Duijnstee, J. M. Ball, V. M. Le Corre, L. J. A. Koster, H. J. Snaith and J. Lim, *ACS Energy Lett.*, 2020, **5**, 376–384.
39 V. M. Le Corre, E. A. Duijnstee, O. El Tambouli, J. M. Ball, H. J. Snaith, J. Lim and L. J. A. Koster, *ACS Energy Lett.*, 2021, **6**, 1087–1094.
40 A. A. Zhumekenov, M. I. Saidaminov, M. A. Haque, E. Alarousu, S. P. Sarmah, B. Murali, I. Dursun, X. H. Miao, A. L. Abdelhady, T. Wu, O. F. Mohammed and O. M. Bakr, *ACS Energy Lett.*, 2016, **1**, 32–37.
41 N. F. Mott and R. T. Gurney, *Paperhound*, 1964, **33**, 275.
42 M. A. Lampert, *Phys. Rev.*, 1956, **103**, 1648–1656.
43 R. D. J. Oliver, P. Caprioglio, F. Peña-Camargo, L. R. V. Buizza, F. Zu, A. J. Ramadan, S. G. Motti, S. Mahesh, M. M. McCarthy, J. H. Warby, Y. H. Lin, N. Koch, S. Albrecht, L. M. Herz, M. B. Johnston, D. Neher, M. Stolterfoht and H. J. Snaith, *Energy Environ. Sci.*, 2022, **15**, 714–726.
44 H. Na, M. Qiang Li, J. Cha, S. Kim, H. Jin, D. Baek, M. Kyong Kim, S. Sim, M. Lee, M. Kim, J. Lim, J. Lee and M. Kim, *Appl. Surf. Sci.*, 2023, **626**, 157209.
45 R. Zheng, S. Zhao, H. Zhang, H. Li, J. Zhuang, X. Liu, H. Li and H. Wang, *Sol. Energy*, 2021, **224**, 472–479.
46 W. Liu, N. Liu, S. Ji, H. Hua, Y. Ma, R. Hu, J. Zhang, L. Chu, X. Li and W. Huang, *Nano–Micro Lett.*, 2020, **12**, 1–11.
47 T. Luo, G. Ye, X. Chen, M. Ding, T. Ye, C. Zhao, W. Zhang and H. Chang, *ACS Appl. Energy Mater.*, 2021, **4**, 12290–12297.
48 A. F. Akbulatov, V. M. Martynenko, L. A. Frolova, N. N. Dremova, I. Zhidkov, S. A. Tsarev, S. Y. Luchkin, E. Z. Kurmaev, S. M. Aldoshin, K. J. Stevenson and P. A. Troshin, *Sol. Energy Mater. Sol. Cells*, 2020, **213**, 110559.
49 M. Long, T. Zhang, M. Liu, Z. Chen, C. Wang, W. Xie, F. Xie, J. Chen, G. Li and J. Xu, *Adv. Mater.*, 2018, **30**, 1–10.
50 R. Chen, Y. Wang, S. N. Khan, F. Xing, S. Li, Y. Rao, H. Wang and Z. Mei, *J. Mater. Chem. A*, 2025, **13**, 9822–9829.
51 L. Hu, W. Zhao, W. Duan, G. Chen, B. Fan and X. Zhang, *Micromachines*, 2022, **13**(3), 457.
52 S. Svanström, T. J. Jacobsson, G. Boschloo, E. M. J. Johansson, H. Rensmo and U. B. Cappel, *ACS Appl. Mater. Interfaces*, 2020, **12**, 7212–7221.
53 F. Bisconti, M. Leoncini, G. Bravetti, A. Giuri, L. Polimeno, S. Carallo, S. Colella, L. Gatto, F. Grandi, E. Cinquanta, C. Vozzi, S. Gambino, L. Dominici and A. Rizzo, *J. Mater. Chem. C*, 2023, **11**, 12213–12221.
54 K. P. Goetz, A. D. Taylor, F. Paulus and Y. Vaynzof, *Adv. Funct. Mater.*, 2020, **30**(23), 191004.
55 R. E. Beal, N. Z. Hagström, J. Barrier, A. Gold-Parker, R. Prasanna, K. A. Bush, D. Passarello, L. T. Schelhas, K. Brüning, C. J. Tassone, H.-G. Steinrück, M. D. McGehee, M. F. Toney and A. F. Nogueira, *Matter*, 2020, **2**, 207–219.
56 Z. Huang, F. Jiang, Z. Song, K. Dolia, T. Zhu, Y. Yan and D. S. Ginger, *ACS Energy Lett.*, 2024, **9**, 3066–3073.
57 E. T. Hoke, D. J. Slotcavage, E. R. Dohner, A. R. Bowring, H. I. Karunadasa and M. D. McGehee, *Chem. Sci.*, 2015, **6**, 613–617.
58 J. Di, J. Chang and S. (Frank) Liu, *EcoMat*, 2020, **2**(3), e12036.
59 D. S. Chung, T. Davidson-Hall, G. Cotella, Q. Lyu, P. Chun and H. Aziz, *Nano–Micro Lett.*, 2022, **14**, 1–15.